Electrical Resistance of Nanochannel-Microchannel Systems: An Exact Solution

Yoav Green,[1,*] Ramadan Abu-Rjal,[2,†] and Ran Eshel[2]
[1] *Department of Mechanical Engineering, Ben-Gurion University of the Negev, Beer-Sheva 8410501, Israel*
[2] *Faculty of Mechanical Engineering, Technion—Israel Institute of Technology, Technion City 3200003, Israel*

(Received 13 November 2019; revised 16 May 2020; accepted 2 June 2020; published 24 July 2020; corrected 5 October 2020)

Current paradigm suggests that the Ohmic electrical response of nanochannel-microchannel systems is determined solely by the nanochannel while the effects of the adjacent microchannels are negligible. However, recent works have challenged this paradigm and have shown that at low concentrations the microchannels contribute in a non-negligible manner. As such, the two favored models used to explain experiments are inadequate in describing realistic nanochannel-microchannel systems. To partially reconcile some of these issues, two newer nanochannel-microchannel models were derived and suggested as a suitable replacement for the nanochannel-dominant models. Unfortunately, these two models are limited to either very low or very high concentrations. In this work, we review these four leading models. We discuss their key assumptions, advantages, shortcomings, and present a knowledge gap between all models pertaining to the effects of the microchannel resistance for all concentrations. To overcome this gap, we derive an analytical solution that accounts for the effects of the microchannels and holds for all concentrations. This solution unifies three of the existing models where we show that they are limiting cases of our more general solution. We are also able to disqualify the fourth model. Our derived solution shows remarkable correspondence to simulations and experiments. The insights from this unifying model can be used to improve the design of any nanofluidic based systems.

DOI: 10.1103/PhysRevApplied.14.014075

I. INTRODUCTION

It has long been thought that the conductance of nanochannel systems (Fig. 1) behaves in a peculiar, yet rather simple-to-understand manner [1,2]. At high concentrations, the conductance, $\tilde{\sigma}$ (tildes denote dimensional quantities), increases linearly with increasing bulk concentration, $\tilde{c}_0$ (i.e., $\tilde{\sigma} \sim \tilde{c}_0$), while at low concentration the resistance saturates to a constant value ($\tilde{\sigma} \sim \text{const}$) determined by the surface charge of the nanochannel itself [dashed red line in Fig. 2(a)]. This behavior has been reported in numerous works [1–46] and reviews [17,47,48].

Two decades ago, with the observation [1,2] of the "saturation-to-linear-increase" behavior, two remarkably simple models were suggested [15,16,21,24,48]. Inherent to these models is the assumption that the overall conductance of a nanochannel-microchannel system (Fig. 1) is determined solely by the nanochannel resistance. Since both models are remarkably simple and intuitive, they have not been challenged nor scrutinized, and as such are still in use [14,33,34,36,38–42,44–46,49].

There is a growing body of evidence [50–54] that challenges this well-accepted "saturation-to-linear-increase" paradigm. Namely, it has been observed that at low concentrations, the conductance does not saturate but rather has a linear ($\tilde{\sigma} \sim \tilde{c}_0$) scaling [solid blue line in Fig. 2(a)]. In contrast to the previous "saturation-to-linear-increase" paradigm, which neglected the effects of the microchannels, the recent approach emphasizes the importance of the microchannels and shows that the $\tilde{\sigma} \sim \tilde{c}_0$ scaling originates due to microchannel effects.

Since the Ohmic response lays at the heart of any nanofluidic based application (electrodialysis [55–59], energy harvesting [3,34–38,51,60–62], fluid-based electrical diodes [4,51,63–67], DNA biosensors [68–75], biomaterial modeling [33], and modeling basic physiological phenomena [76]) that span all nanoporous material (graphene-oxide-based membranes [5,14,25–27,40,77], carbon nanotubes [20,78,79], silicon nanochannels and nanopores [6,39,46,52,80,81], conducting hydrogels [33], colloid-based membranes [7,8,41], mesoporous silica films [28], exfoliated layers of a clay mineral [29], Nafion [82], cellulose nanofiber membrane from wood [30,42], Ti_3C_2 MXene membranes [9,35,36], MXene/Kevlar membranes [34], single-layer MoS_2 nanopores [18], AMX-Sb anion exchange membranes [83–85], and more [38,43,44]), it is crucial to revisit the nanochannel conductance "saturation-to-linear-increase" paradigm suggested two decades ago and reconcile the apparent inconsistency between the original "saturation-to-linear-increase" paradigm to the

---

[*] yoavgreen@bgu.ac.il
[†] ramadan.rjal@campus.technion.ac.il

© 2020 American Physical Society

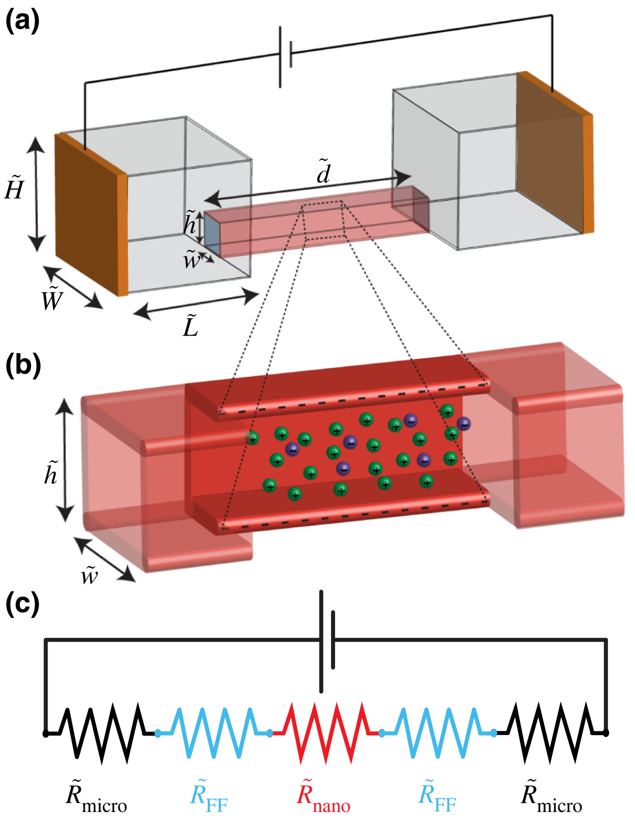

FIG. 1. (a) 3D schematic representation of a nanochannel-microchannel system with two electrodes at the ends connected to a power source. The interfaces of the microchannels and nanochannel are marked by blue and correspond to the field-focusing resistors, $\tilde{R}_{\mathrm{FF}}$, described below. (b) In the enlargement of the permselective nanochannel cross section it can be observed that there is a surplus of positive ions (green spheres) relative to the negative ions (purple spheres). This is due to the negative surface charge. (c) Equivalent electrical circuit of the nanochannel-microchannel system. The red permselective region schematically describes the behavior of ions in any material that exhibits permselectivity such that the electrical circuit model holds for any system that exhibits permselectivity.

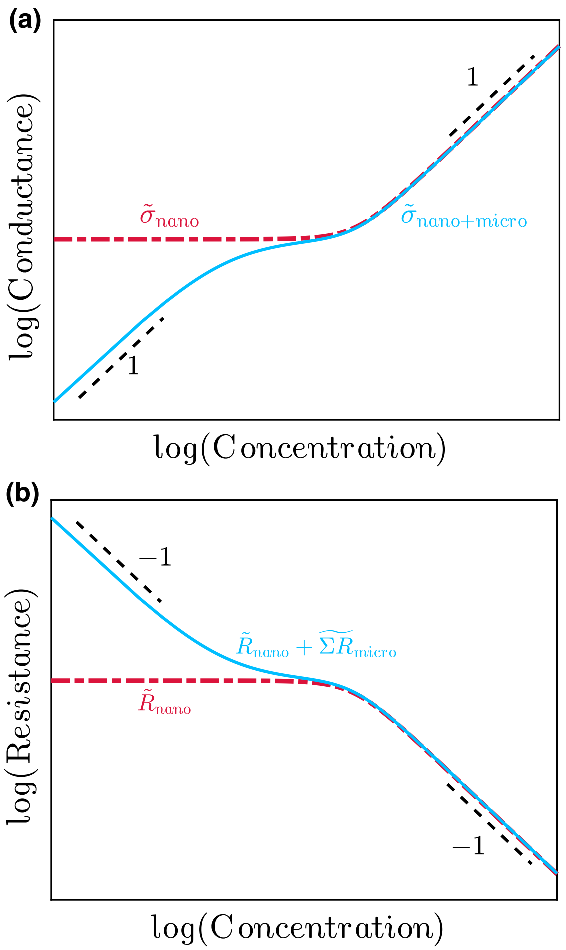

FIG. 2. Log-log plot of the (a) total electrical conductance, $\tilde{\sigma}$, and (b) total electrical resistance, $\tilde{R}$, versus the concentration. The conductance and resistance are related by $\tilde{\sigma}=\tilde{R}^{-1}$. Both figures plot the nanochannel-dominated system, $\tilde{R}_{\mathrm{nano}}$, and a system accounting for both the nanochannel and the various microchannel resistances, $\tilde{R}_{\mathrm{nano}}+\widetilde{\Sigma R}_{\mathrm{micro}}$. The black dashed lines here and elsewhere denote a slope of either 1 or −1.

more recent understandings of the "linear-increase-to-saturation-to-linear-increase" paradigm.

On the one hand, there is abundant evidence supporting the older paradigm (see all of the above-mentioned works, notably recent works [14,33,34,36,38–42,44–46,49]). As with any well-established paradigm it is difficult to question and/or challenge it. Yet, on the other hand, the newer paradigm suggested by theory [50,51] has been confirmed by numerical simulations [50,53] and experiments [52,54]. As such, a resolution between these two approaches is needed. This resolution is the main finding of this work. We demonstrate that the older "saturation-to-linear-increase" paradigm is but a limiting scenario of the more general "linear-increase-to-saturation-to-linear-increase" paradigm. Thus, the theoretical findings suggested in this work are not in contradiction to past findings but rather they supplement them.

In this work, we address the following questions. (1) Which of the previously mentioned two nanochannel-dominant models is the correct one and why? (2) Why do both models fail at lower concentrations when the effects of the microchannels are non-negligible? (3) Can the different models (nanochannel-dominant and nanochannel-microchannel models) be reconciled? And if so, how? To answer these questions, we first present the four leading models: two "saturation-to-linear-increase" models that ignore the effects of the microchannels and two "linear-increase-to-saturation-to-linear-increase" models that account for the effects of the microchannels. We discuss the key underlying assumptions of each model, as well as their advantages, and their shortcomings and limitations. We show that there is a knowledge gap between all these models. Thereafter, we derive an analytical solution that bridges this gap by unifying three of the models and disqualifying the other leading nanochannel-dominant model. This unifying model, which is described by two simple equations, explains why the "saturation-to-linear-increase" paradigm fails at lower concentration but also unifies it with the "linear-increase-to-saturation-to-linear-increase" paradigm. We believe that the findings of this work will substantially improve the design of nanofluidic based applications, many of which are pressing to society.

The paper is divided as follows. Section II presents and discusses the four leading models. In Sec. III we derive our unifying solution. In Sec. IV we discuss the key findings of this work. Finally, in Sec. V we conclude with a few short remarks.

II. LEADING MODELS

In this section we present and discuss the leading models. But before that, to better understand the transition from a linear dependence on the concentration to a saturation, one needs to discuss how a property termed permselectivity changes with the concentration. Permselectivity is the ability of nanochannels to filter out ions of a particular charge (positive or negative) [17,63,86]. It is controlled by the degree of the Debye length overlap of two surfaces as well as the excess counterion concentration in the channel, $\tilde{N}$ (which is related to the surface charge, an exact expression relating these quantities is given below) [67,87–89]. The degree to which a system is permselective is characterized by the transport number (described below) [90] and ranges from two extreme cases: ideal permselectivity [low concentrations – $N = \tilde{N}/\tilde{c}_0 \gg 1$ (quantities without tildes are dimensionless)] and vanishing permselectivity (high concentrations – $N \ll 1$).

How much a system needs to be permselective (or not at all) depends on the desired applications. Regardless of application, both ideal and vanishing permselective systems share a common feature: at small currents and for all concentrations, the current-voltage ($\tilde{I}$ - $\tilde{V}$) response is linear. For ideal permselectivity and larger currents, the response is no longer linear [50–52,55–57,87–93]. Herein, we focus only on the linear Ohmic resistance.

In the literature it is common to discuss the behavior of the electrical conductance of the system, denoted by $\tilde{\sigma} = \tilde{I}/\tilde{V}$. In this work we almost solely discuss the electrical resistance, which is reciprocal to the conductance ($\tilde{R} = \tilde{\sigma}^{-1} = \tilde{V}/\tilde{I}$). The advantages of the resistance approach becomes apparent shortly. Figure 2 depicts the behavior of both the conductance and resistance. In the resistance approach the "saturation-to-linear-increase" conductance paradigm is replaced with a "saturation-to-linear-decrease" resistance paradigm and the "linear-increase-to-saturation-to-linear-increase" conductance paradigm is replaced with a "linear-decrease-to-saturation-to-linear-decrease" resistance paradigm.

A. One-layer system—superposition model

Perhaps the most popularly used model is the one we denote as the "superposition model." This model was suggested by Schoch *et al.* [15–17] and since then has been adopted by many [3–14,31–34,36,38–42,44–47,49]. It has been further extended to account for additional phenomena [18,19,54]. This model is based on two key assumptions: (1) the overall response of the system is solely determined by the nanochannel. (2) The total conductance is a superposition of two different states described in the paragraph below.

It is known that the electrical current passing through the nanochannel depends on the geometry and the local conductivity, $\tilde{\kappa}$. This conductance, where only the bulk concentration varies, is commonly termed bulk conductance, $\tilde{\sigma}_{\text{bulk}}$, and is defined by $\tilde{\sigma}_{\text{bulk}} = 2\tilde{\kappa}\tilde{h}\tilde{w}/\tilde{d}$ where $\tilde{d}$, $\tilde{h}$, and $\tilde{w}$ are the length, height, and width of the nanochannel, respectively (Fig. 1). It was suggested that the total conductance is further increased by the contribution of the current transported due to the surface charge, $\tilde{\sigma}_s$, or excess counterion concentration $\tilde{N} = -2\tilde{\sigma}_s/\tilde{F}\tilde{h}$, where $\tilde{F}$ is the Faraday constant. This contribution is termed surface conductance and is given by $\tilde{\sigma}_{\text{surface}} = \tilde{\kappa}\tilde{N}\tilde{h}\tilde{w}/(\tilde{c}_0\tilde{d})$. It is assumed that the total conductance of the nanochannel is simply a superposition of these two states

$$\tilde{R}^{-1}_{1,\text{super}} = \tilde{\sigma}_{1,\text{super}} = \tilde{\sigma}_{\text{bulk}} + \tilde{\sigma}_{\text{surface}} = \frac{\tilde{h}\tilde{w}}{\tilde{\rho}_{\text{res}}\tilde{d}}\left(2 + \frac{\tilde{N}}{\tilde{c}_0}\right), \tag{1}$$

where $\tilde{\rho}_{\text{res}}$ is the local resistivity and is given by $\tilde{\rho}_{\text{res}} = \tilde{\kappa}^{-1} = \tilde{\Re}\tilde{T}/\tilde{F}^2\tilde{D}\tilde{c}_0$. Here, $\tilde{\Re}$ is the universal gas constant, $\tilde{T}$ is the absolute temperature, and $\tilde{D}$ is the diffusion coefficient. The subscript for the resistance, here and below, is comprised of two components, number and name. The number denotes the number of layers within the system (e.g., in this case it is one layer, only the nanochannel) and the name denotes the model (for brevity, we use the shortened subscript *super* to denote superposition).

Advantages. The form of Eq. (1) suggests that these two contributions describe two resistors connected in parallel implying that there are two separate routes for current transport. More importantly, regardless of the intuitive physical interpretation provided, the model is conceptually easy to understand and Eq. (1) is simple to implement.

Shortcomings. Perhaps the greatest advantage of the superposition approach is also its greatest disadvantage—it is intuitive and relies on the assumption that if both limits of high and low concentrations hold then a superposition of these states holds for all concentrations. However, careful inspection and comparison of $\tilde{R}_{1,\text{super}}$ with one-dimensional (1D) simulations (Fig. 3) shows that the correspondence at the intermediate value of $\tilde{N} \sim \tilde{c}_0$, where the superposition assumption is the intended resolution, is not good. This unfortunate shortcoming is unique to this model, compared to the other models discussed below: these other models can be rigorously derived from the Poisson-Nernst-Planck equations, while for this model [Eq. (1)] there is no known derivation. Rather $\tilde{R}_{1,\text{super}}$ rests on empirical reasoning, namely, that the superposition of the bulk and surface conduction states is allowable. In fact, it can be shown that these two states are the solutions of the two extreme cases of ideal and vanishing permselectivity. However, the governing equations at these two extremities are different [50]. Yet, using the superposition approach requires that the governing equations be the same. As such, our results suggest that the superposition approach requires re-examination.

B. One-layer system—Donnan equilibrium

This model also assumes that the overall response is determined solely by the nanochannel. However, here it is assumed that the nanochannel is in Donnan equilibrium with its environment. This resistance is given by [20,21,48]

$$\tilde{R}_{1,\text{Donnan}} = \frac{\tilde{\rho}_{\text{res}}\tilde{d}}{\tilde{h}\tilde{w}} \frac{1}{\sqrt{4+N^2}}, \tag{2}$$

and once more $N = \tilde{N}/\tilde{c}_0$ is the nondimensional excess counterion concentration.

Advantages. Figure 3 demonstrates that Eq. (2) has perfect correspondence to the 1D simulations for the entire range of $\tilde{c}_0$. This is unsurprising, as this model can be analytically derived from the Poisson-Nernst-Planck equations.

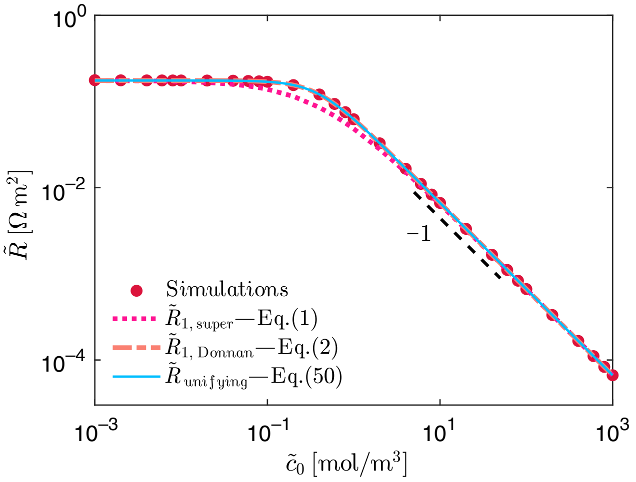

FIG. 3. Log-log plot of the resistance, $\tilde{R}$, versus concentration, $\tilde{c}_0$, of a 1D one-layered system ($\tilde{L} = 0$, i.e., no microchannels). Simulation data taken from Ref. [52] and simulation parameters are given in the Appendix.

Shortcomings. In deriving this solution, it is assumed that the electrodes are placed exactly at the nanochannel interfaces, such that the microchannel length is zero, $\tilde{L} = 0$, and that the adjoining microchannel-resistance contribution is negligible. Hence, when $\tilde{L} \neq 0$, this model and the superposition model are incapable of describing the observed additional increase of the resistance with decreasing concentration [1D simulations of nanochannel-microchannels—see Fig. 2 of Ref. [52], two-dimensional (2D) simulations—Fig. 4, and three-dimensional (3D) experiments—Fig. 5].

C. Three-layer system—ideal and vanishing permselectivity

Similar to the above model, this model also satisfies the Donnan equilibrium of the nanochannel. However, here this equilibrium is not with the bulk environments but rather with the microchannels such that the resistance contributions of the adjoining microchannels are explicitly accounted for [50–52]. In contrast to the two previous models that hold for all concentrations, these models are limited to the two extreme cases corresponding to ideal permselectivity ($N \gg 1$) and vanishing permselectivity ($N \ll 1$). The expressions for the resistances are [50–52]

$$\tilde{R}_{3,\text{vanishing}} = \tfrac{1}{2}(\tilde{R}_{\text{nano}} + \widetilde{\Sigma R}_{\text{micro}}), \tag{3}$$

$$\tilde{R}_{3,\text{ideal}} = \tilde{\tilde{R}}_{\text{nano}} + \widetilde{\Sigma R}_{\text{micro}}, \tag{4}$$

where

$$\tilde{R}_{\text{nano}} = \frac{\tilde{\rho}_{\text{res}}\tilde{d}}{\tilde{h}\tilde{w}}, \quad \tilde{\tilde{R}}_{\text{nano}} = \frac{\tilde{R}_{\text{nano}}}{N}, \tag{5}$$

$$\widetilde{\Sigma R}_{\text{micro}} = 2(\tilde{R}_{\text{micro}} + \tilde{R}_{\text{FF}}), \quad \tilde{R}_{\text{micro}} = \frac{\tilde{\rho}_{\text{res}}\tilde{L}}{\tilde{H}\tilde{W}},$$
$$\tilde{R}_{\text{FF}} = \frac{2\tilde{\rho}_{\text{res}}\tilde{f}}{\tilde{L}}. \tag{6}$$

Here $\tilde{L}$, $\tilde{H}$, and $\tilde{W}$ are the length, height, and width of the microchannels, respectively (Fig. 1). The resistance attributed to the microchannel regions, $\widetilde{\Sigma R}_{\text{micro}}$ [Eq. (6)], is comprised of two contributions [50–52]: (1) a resistance attributed to the rectangular geometry of the system, $\tilde{R}_{\text{micro}}$, which has a similar scaling to the nanochannel resistance, $\tilde{R}_{\text{nano}}$, i.e., it is proportional to the length divided by the cross-section area; (2) a resistance attributed to the focusing of field lines from the larger microchannels into the smaller nanochannel, $\tilde{R}_{\text{FF}}$ (the expression for $\tilde{f}$ is given below). Here, for the sake of simplicity, we consider the case where the microchannels are identical. This need not be the case [50,51]. In the derivation of the unifying resistance (Sec. III) a more general expression, accounting for geometric asymmetries, is given. Two important comments should be made. First, the transition of $\tilde{R}_{3,\text{vanishing}}$ to $\tilde{R}_{3,\text{ideal}}$ with decreasing concentration is attributed to the variation of the counterion transport number, τ. The transport number, defined as the ratio of the flux of the counterions to the total current density, is a major transport characteristic of a permselective system. For an ideal binary system, only counterions are transported through the nanochannel, such that their transport number equals unity ($\tau_{N\gg 1} = 1$) and the nanochannel resistance, $\tilde{\tilde{R}}_{\text{nano}}$, depends on $\tilde{N}$ yet is independent of $\tilde{c}_0$. For a nonideal system, the counterion transport number lies between one-half and unity, $\tau \in [\frac{1}{2}, 1]$. At the other extreme of vanishing permselectivity ($N \ll 1$), the transport number equals one-half ($\tau_{N\ll 1} = \frac{1}{2}$) and the nanochannel resistance, $\tilde{R}_{\text{nano}}$, depends inversely on $\tilde{c}_0$ yet is independent of $\tilde{N}$.

Second, we note that for the case that $\widetilde{\Sigma R}_{\text{micro}} = 0$ (i.e., when the effects of the microchannels are negligible) the expressions for $\tilde{\tilde{R}}_{\text{nano}}$ and $\tilde{R}_{\text{nano}}$ [Eq. (5)] are the limiting expressions of $\tilde{R}_{1,\text{Donnan}}$ [Eq. (2)] for low and high concentrations, respectively. For $\widetilde{\Sigma R}_{\text{micro}} = 0$ two requirements need to be satisfied separately: (1) the microchannel resistance is negligible, $\tilde{R}_{\text{micro}} = 0$. This occurs when the cross-section area is much larger than the length of this systems—for example, a nanochannel that is not connected to small microchannels but rather connected to very large or semi-infinite bulk regions. (2) The effects of field focusing are negligible, $\tilde{R}_{\text{FF}} \sim \tilde{f} \sim 0$. This resistance is attributed to the focusing of field lines from the microchannels to the permselective material. While this resistance depends on the ratio of the nanochannel to microchannels, it is also dependent on the heights and widths of the nanochannels and microchannels. Hence for macroscopically large systems where the heights and widths are large (such as the various membranes discussed above), the ratio of $\tilde{R}_{\text{FF}}$ to $\tilde{\tilde{R}}_{\text{nano}}$ is negligible.

Shortcomings. Each model is limited to either $N \ll 1$ or $N \gg 1$. As can be expected, the solution in the $N \sim 1$ region, where the two models intercept (2D simulations—Fig. 4, and 3D experiments—Fig. 5), is only approximate.

Advantages. First, the derivation of the exact solution from the Poisson-Nernst-Planck equations for the two extreme cases, ideal and vanishing permselectivity, is relatively simple and straightforward [50–52]. Second, while in this work we only consider the Ohmic response, the solution for ideal permselectivity also holds for the limiting current, $\tilde{I}_{\text{lim}}$, regime where the $\tilde{I}$ - $\tilde{V}$ response is no longer linear [51,67,80]. Third, and perhaps the greatest advantage, these models have excellent correspondence with 2D simulations (Fig. 4) and 3D experiments [52] (Fig. 5). Finally, these models provide a very clear and simple physical picture and interpretation—the total resistance of the system is that of a series of resistances [Fig. 1(c)]. In the resistance formulation the removal or addition of one component or resistor is intuitive or straightforward, which is yet another added benefit of the resistance formulation.

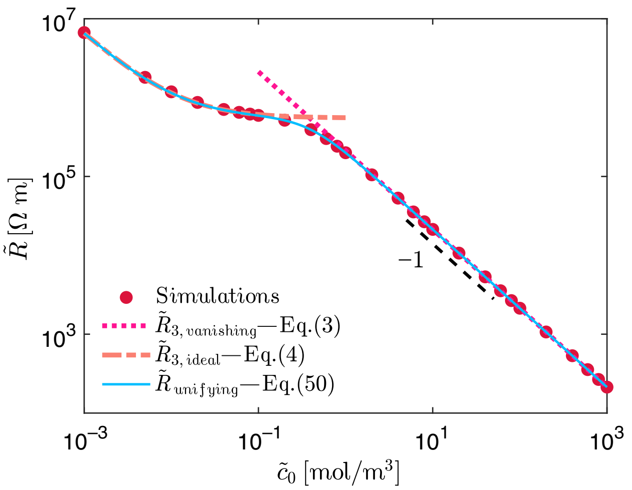

FIG. 4. Log-log plot of the resistance, $\tilde{R}$, versus concentration, $\tilde{c}_0$, of a three-layered (two microchannels connected by a nanochannel) 2D system. Simulation data taken from Ref. [50]. Simulation parameters are given in the Appendix.

D. Limitations

Thus far we present four leading models: two models that hold for all concentrations but assume that the effects of the microchannels are negligible ($\tilde{R}_{1,\text{super}}$ and

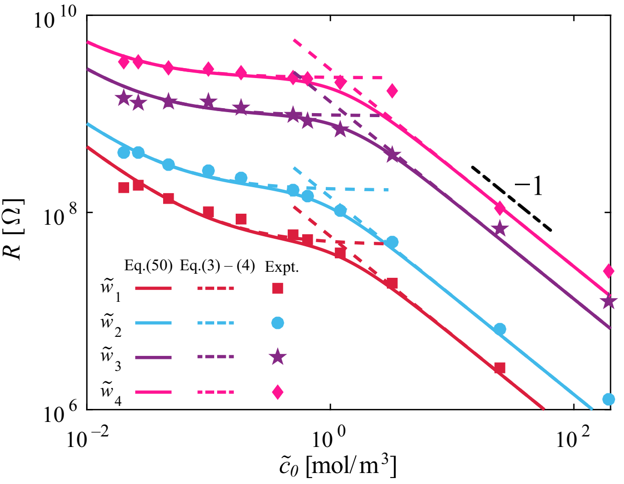

FIG. 5. Log-log plot of the resistance, $\tilde{R}$, versus concentration, $\tilde{c}_0$, of 3D experiments of a three-layered system for four different nanochannels of decreasing width ($\tilde{w}_1 > \tilde{w}_2 > \tilde{w}_3 > \tilde{w}_4$). Experimental data is taken from Ref. [52]. Additional geometric details are given in the Appendix.

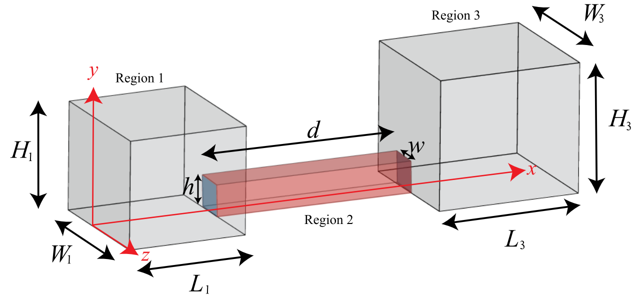

FIG. 6. 3D schematic plot of the general case of a microchannel-nanochannel system, where the microchannels (region 1 and region 3) are not symmetric. The remaining details are similar to those given in Fig. 1. The red $\hat{x}$ axis line runs along the center of the microchannels and nanochannel (region 2) when $y = 0, z = 0$.

$\tilde{R}_{1,\text{Donnan}}$) and two models that account for the effects of the microchannels but are limited in concentration range ($\tilde{R}_{3,\text{ideal}}$ and $\tilde{R}_{3,\text{vanishing}}$). Table I provides a summary of these models. In the next section we present the derivation of our model, $\tilde{R}_{\text{unifying}}$, that unifies three of these models ($\tilde{R}_{1,\text{Donnan}}$, $\tilde{R}_{3,\text{ideal}}$, and $\tilde{R}_{3,\text{vanishing}}$). The summary of $\tilde{R}_{\text{unifying}}$ is given here as well.

III. SOLUTION DERIVATION

A. Model geometry

The geometry of the problem is defined in Fig. 6 where we consider the more general case in which the microchannels are not necessarily symmetric. In contrast to Fig. 1, the electrodes have been removed to allow for the simple visualization of the origin on the left. We use the following notations to denote lengths within the system

$$\Delta_1 = L_1,\ \Delta_2 = \Delta_1 + d,\ \Delta_3 = \Delta_2 + L_3. \tag{7}$$

Similar to Fig. 1, we do use the same definition for positive and negative voltages. The leftmost region where a positive applied potential, $V > 0$, results in a positive electrical current, $I > 0$, is defined as region 1. Region 1 is defined in $x \in [0, \Delta_1]$, $y \in [0, H_1]$, $z \in \frac{1}{2}[-W_1, W_1]$. Region 2 is the permselective region and is defined in $x \in [\Delta_1, \Delta_2]$, $y \in [0, h]$, $z \in \frac{1}{2}[-w, w]$. The rightmost region is denoted by region 3 and is defined in $x \in [\Delta_2, \Delta_3]$, $y \in [0, H_3]$, $z \in \frac{1}{2}[-W_3, W_3]$. Also, we note that the x axis runs along the center of both the microchannels and the nanochannel for $y = 0, z = 0$.

B. Governing equations

The nondimensional equations governing steady-state ion transport through permselective medium for a symmetric and binary electrolyte ($z_\pm = \pm 1$, $\tilde{D}_\pm = \tilde{D}$) are the Poisson-Nernst-Planck (PNP) equations

$$\nabla \cdot (\nabla c_+ + c_+ \nabla \phi) = -\nabla \cdot \mathbf{j}_+ = 0, \tag{8}$$

$$\nabla \cdot (\nabla c_- - c_- \nabla \phi) = -\nabla \cdot \mathbf{j}_- = 0, \tag{9}$$

$$2\varepsilon^2 \nabla^2 \phi = -\rho_e = -(c_+ - c_- - N\delta_{2,k}). \tag{10}$$

Equations (8) and (9) are the Nernst-Planck equations satisfying continuity of ionic fluxes for the cation and anion concentrations c_+ and c_-, respectively. The current densities are given accordingly by $\mathbf{j}_\pm$. Equation (10) is the Poisson equation for the electric potential ϕ. The inhomogeneous term of Eq. (10) is the space-charge density, where δ_{2k} is Kronecker's delta, $k = 1, 2, 3$ denote each region, and $N > 0$ is the fixed volumetric charge density accounting for the (negative) surface charge within the permselective region. The variables in Eqs. (8)–(10) are normalized by the following quantities (once more, tildes denote dimensional quantities)

$$\tilde{c}_\pm = c_\pm \tilde{c}_0, \tilde{N} = N\tilde{c}_0, \tilde{\phi} = \phi\tilde{\phi}_{th}, \tilde{\mathbf{x}} = \mathbf{x}\tilde{L}, \tilde{\mathbf{j}} = \mathbf{j}\tilde{D}\tilde{c}_0\tilde{L}^{-1}, \tag{11}$$

TABLE I. Summary of assumptions, advantages, and limitations of all models.

	Derivable[a]	Geometry[b]	Concentration[c]	Current[d]	Sim/Expt.[e]
$\tilde{R}_{1,\text{super}}$	No	$\tilde{L} = 0$	All $\tilde{c}_0$	$\tilde{I} \ll \tilde{I}_{\text{lim}}$	No
$\tilde{R}_{1,\text{Donnan}}$	Yes	$\tilde{L} = 0$	All $\tilde{c}_0$	$\tilde{I} \ll \tilde{I}_{\text{lim}}$	Yes
$\tilde{R}_{3,\text{ideal}}$	Yes	None	$\tilde{N} \gg \tilde{c}_0$	$\tilde{I}_{\text{lim}}$	Yes
$\tilde{R}_{3,\text{vanishing}}$	Yes	None	$\tilde{N} \ll \tilde{c}_0$	$\tilde{I} \ll \tilde{I}_{\text{lim}}$	Yes
$\tilde{R}_{\text{unifying}}$	Yes	None	All $\tilde{c}_0$	$\tilde{I} \ll \tilde{I}_{\text{lim}}$	Yes

[a] Model can be derived from Poisson-Nernst-Planck equations.
[b] Geometric limitations.
[c] Concentration range limitations.
[d] Current range limitations (Ohmic response, $\tilde{I} \ll \tilde{I}_{\text{lim}}$; limiting current, $\tilde{I}_{\text{lim}}$).
[e] Good correspondences with simulations and/or experiments.

where $\tilde{c}_0$ is the bulk concentration, $\tilde{D}$ is the diffusion coefficient, and $\tilde{L}$ is a characteristic length, which can be any of the lengths within the system (see Ref. [50]). The thermal electric potential is given by $\tilde{\phi}_{\mathrm{th}} = \tilde{\Re}\tilde{T}/\tilde{F}$, where $\tilde{\Re}$, $\tilde{T}$, and $\tilde{F}$ are, respectively, the universal gas constant, absolute temperature, and Faraday constant. Equation (11) naturally leads to the normalized Debye length

$$\varepsilon = \frac{\tilde{\lambda}_D}{\tilde{L}}, \quad \tilde{\lambda}_D = \sqrt{\frac{\tilde{\varepsilon}_0 \varepsilon_r \tilde{\Re}\tilde{T}}{2\tilde{F}^2 \tilde{c}_0}}, \tag{12}$$

where $\tilde{\varepsilon}_0$ and ε_r are the permittivity of vacuum and the relative permittivity of the electrolyte, respectively.

Henceforth, we use the assumption of local electroneutrality (LEN) in the system whereby $\varepsilon \to 0$ such that $\varepsilon^2 \nabla^2 \phi \ll 1$. This results in $\rho_e = 0$ in all three regions. In regions 1 and 3 we obtain

$$c_+ = c_- = c_{1,3}, \tag{13}$$

while in region 2, we obtain

$$c_{2,-} = c_2, \quad c_{2,+} = c_2 + N. \tag{14}$$

In Sec. III C we present the solution in the microchannels (regions 1 and 3), and in Sec. III D we derive the solution in the nanochannel (region 2).

C. Solution for regions 1 and 3

Adding and subtracting Eqs. (8) and (9) yields, upon using the LEN condition, Eq. (13) (and dropping the 1,3 subscripts)

$$\nabla^2 c = -\tfrac{1}{2}\nabla \cdot \mathbf{j} = 0, \tag{15}$$

$$\nabla \cdot (c\nabla\phi) = -\tfrac{1}{2}\nabla \cdot \mathbf{i} = 0, \tag{16}$$

where

$$\mathbf{j} = \mathbf{j}_+ + \mathbf{j}_-, \quad \mathbf{i} = \mathbf{j}_+ - \mathbf{j}_-, \tag{17}$$

are the salt current densities and electrical current densities, respectively. In contrast to $\mathbf{j}$, which has been normalized by $\tilde{D}\tilde{c}_0\tilde{L}^{-1}$, $\mathbf{i}$ has been normalized by $\tilde{F}\tilde{D}\tilde{c}_0\tilde{L}^{-1}$.

For the sake of brevity, we provide here the final solution for c_1, c_3, ϕ_1, ϕ_3 and refer the interested readers to the following works. The derivation of the 3D concentration and electric potential distributions for the case of $\mathbf{i} = \mathbf{j} = \mathbf{j}_+$ (and $\mathbf{j}_- \triangleq 0$) can be found in Refs. [50,94]. In contrast to Refs. [50,94], which primarily considered ideal permselective medium ($\mathbf{j}_- \triangleq 0$), Ref. [90] considered the more general case, as considered here, where $\mathbf{j}_- \neq 0$. Combining the approaches of Refs. [50,94] with Ref. [90] yields the following distributions for $c_1(x,y,z)$ and $c_3(x,y,z)$:

$$\begin{aligned}
c_1(x,y,z) = {} & 1 - \frac{J}{2W_1H_1}x - \frac{4J}{whW_1H_1}\sum_{n,m=1}^{\infty}\frac{\sin[\lambda_n{}^{(1)}h]\sin[\gamma_m{}^{(1)}w/2]}{\kappa_{n,m}{}^{(1)}\lambda_n{}^{(1)}\gamma_m{}^{(1)}\cosh[\kappa_{n,m}{}^{(1)}L_1]}\cos[\lambda_n{}^{(1)}y]\cos[\gamma_m{}^{(1)}z]\sinh[\kappa_{n,m}{}^{(1)}x] \\
& - \frac{J}{hW_1H_1}\sum_{n=1}^{\infty}\frac{\sin[\lambda_n{}^{(1)}h]}{[\lambda_n{}^{(1)}]^2\cosh[\lambda_n{}^{(1)}L_1]}\cos[\lambda_n{}^{(1)}y]\sinh[\lambda_n{}^{(1)}x] \\
& - \frac{2J}{wW_1H_1}\sum_{m=1}^{\infty}\frac{\sin[\gamma_m{}^{(1)}w/2]}{[\gamma_m{}^{(1)}]^2\cosh[\gamma_m{}^{(1)}L_1]}\cos[\gamma_m{}^{(1)}z]\sinh[\gamma_m{}^{(1)}x],
\end{aligned} \tag{18}$$

$$\begin{aligned}
c_3(x,y,z) = {} & 1 + \frac{J}{2W_3H_3}(\Delta_3 - x) + \frac{4J}{whW_3H_3}\sum_{n,m=1}^{\infty}\frac{\sin[\lambda_n{}^{(3)}h]\sin[\gamma_m{}^{(3)}w/2]}{\kappa_{n,m}{}^{(3)}\lambda_n{}^{(3)}\gamma_m{}^{(3)}\cosh[\kappa_{n,m}{}^{(3)}L_3]} \\
& \times \cos[\lambda_n{}^{(3)}y]\cos[\gamma_m{}^{(3)}z]\sinh[\kappa_{n,m}{}^{(3)}(\Delta_3 - x)] \\
& + \frac{J}{hW_3H_3}\sum_{n=1}^{\infty}\frac{\sin\lambda_n{}^{(3)}h}{[\lambda_n{}^{(3)}]^2\cosh\lambda_n{}^{(3)}L_3}\cos[\lambda_n{}^{(3)}y]\sinh[\lambda_n{}^{(3)}(\Delta_3 - x)] \\
& + \frac{2J}{wW_3H_3}\sum_{m=1}^{\infty}\frac{\sin[\gamma_m{}^{(3)}w/2]}{[\gamma_m{}^{(3)}]^2\cosh[\gamma_m{}^{(3)}L_3]}\cos[\gamma_m{}^{(3)}z]\sinh[\gamma_m{}^{(3)}(\Delta_3 - x)],
\end{aligned} \tag{19}$$

where the eigenvalues are defined by

$$\lambda_n{}^{(k)} = \frac{\pi n}{H_k},\ \gamma_m{}^{(k)} = \frac{2\pi m}{W_k},$$
$$\kappa_{nm}{}^{(k)} = \sqrt{[\lambda_n{}^{(k)}]^2 + [\gamma_m{}^{(k)}]^2}, \quad k = 1, 3, \tag{20}$$

the current densities and the currents are related by

$$I = i \cdot hw,\ J = j \cdot hw, \tag{21}$$

and the electric potential distributions are [50,51,67,90,95]

$$\phi_1 = \frac{I}{J}\ln c_1 + V,\ \phi_3 = \frac{I}{J}\ln c_3. \tag{22}$$

In 3D, J is normalized by $\tilde{D}\tilde{c}_0\tilde{L}$ while I is normalized by $\tilde{F}\tilde{D}\tilde{c}_0\tilde{L}$. In 2D, J is normalized by $\tilde{D}\tilde{c}_0$ while I is normalized by $\tilde{F}\tilde{D}\tilde{c}_0$. In the remainder of this work, for the sake of brevity and based on notational convenience, we use both currents (I, J) and current densities (i,j). These are trivially related by Eq. (21).

It should be noted that the solution given by Eqs. (18)–(20) is different than those given in previous works. Here we consider the case that regions 1 and 3 are defined in $y \in [0, H_k]$, $z \in \frac{1}{2}[-W_k, W_k]$ (as well as $x_1 = x \in [0, \Delta_1]$ and $x_3 = x \in [\Delta_2, \Delta_3]$) and the permselective interface is defined in $y \in [0, h]$, $z \in \frac{1}{2}[-w, w]$. Previous 3D works [50,94] considered half cells where the regions were defined in $y \in [0, H_k]$, $z \in [0, W_k]$ (with similar x_1 and x_3) and the permselective interface was in $y \in [0, h]$, $z \in [0, w]$ while 2D works [51,67,90,96] considered the simpler case where the region was defined in $x \in [0, L_k]$, $y \in [0, H_k]$ and the permselective region in $y \in [0, h]$. As a result, the coefficients of the third and fifth terms of Eqs. (18) and (19) and the eigenvalues $\gamma_m{}^{(k)}$ of Eq. (20) are modified relative to those presented in Refs. [50,94]. They are multiplied by an additional factor of 2.

In the remainder of this derivation, all that is needed is the concentration distributions at the two permselective interfaces $x = \Delta_1, \Delta_2$ [Eq. (7)] denoted by

$$\bar{c}_1 = c_1(\Delta_1, 0, 0) = 1 - \frac{JL_1}{2W_1H_1} - Jf_1(L_1),$$
$$\bar{c}_3 = c_3(\Delta_2, 0, 0) = 1 + \frac{JL_3}{2W_3H_3} + Jf_3(L_3). \tag{23}$$

The expressions for the $f_k(L_k)$, also termed field-focusing resistors, are defined from Eqs. (18) and (19), and their behavior has been investigated in previous works [50–52,67,80,94,96]. Throughout, we denote the concentration at the permselective interfaces with an overbar.

D. Region 2 solution and *I* - *J* relation

Due to the requirement that the channels walls are impermeable for ions ($\mathbf{j}_\pm \cdot \mathbf{n} = 0$) [50,51,67] and under the assumption that the channels are long such that the currents are "fully developed" as in traditional pipe flows, the governing equations can be reduced to 1D (in the x axis). Thus, after taking the sum and difference of Eqs. (8) and (9) along with Eq. (14), the governing equations in region 2 become

$$2c_{2,x} + N\phi_{,x} = -j, \tag{24}$$

$$(2c_2 + N)\phi_{,x} = -i, \tag{25}$$

where $()_{,x}$ denotes the x derivative. Isolating $\phi_{,x}$ yields

$$2c_{2,x} - \frac{Ni}{2c_2 + N} = -j, \tag{26}$$

which can be rewritten as

$$\frac{2(2c_2 + N)}{Ni - j(2c_2 + N)}\frac{dc_2}{dx} = 1. \tag{27}$$

Integration of Eq. (27) over the segment $x \in [\Delta_1, \Delta_2]$ yields

$$\left\{c_2 + \frac{iN}{2j}\log[(i - j)N - 2c_2 j]\right\}_{\bar{c}_{21}}^{\bar{c}_{23}} = -\frac{jd}{2}, \tag{28}$$

where $\bar{c}_{23} = c_2(\Delta_2, 0, 0)$ and $\bar{c}_{21} = c_2(\Delta_1, 0, 0)$ are currently unknown. However, $\bar{c}_{21}$ and $\bar{c}_{23}$ can be related to $\bar{c}_1$ and $\bar{c}_3$ [Eq. (23)] via the electrochemical potentials

$$\mu_\pm = \ln c_\pm \pm \phi, \tag{29}$$

by requiring that both positive and negative electrochemical potentials are continuous at the two permselective interfaces $(x = \Delta_1, \Delta_2)$. It is advantageous to take the sum of both $(\mu = \mu_+ + \mu_-)$, as this can be translated to requiring continuity of $\mu = \ln c_+ c_-$ at both interfaces. Then, using Eqs. (14), (23), and (29) yields

$$\bar{c}_{2k}(\bar{c}_{2k} + N) = \bar{c}^2_{k=1,3}, \tag{30}$$

which can be solved for the interfacial concentrations within region 2

$$\bar{c}_{21} = -\frac{N}{2} + \sqrt{\frac{N^2}{4} + \bar{c}_1^2}, \quad \bar{c}_{23} = -\frac{N}{2} + \sqrt{\frac{N^2}{4} + \bar{c}_3^2}. \tag{31}$$

Note that using $\mu = \ln c_+ c_-$ thus far is equivalent to using only one boundary condition. The other is used shortly in the derivation of the current-voltage relations [see Eq. (36)].

Inserting Eq. (31) into Eq. (28), yields the following i - j (or I - J) relation

$$\frac{iN}{2j}\ln\left(\frac{iN - j\sqrt{N^2+4\bar{c}_3^2}}{iN - j\sqrt{N^2+4\bar{c}_1^2}}\right) = \sqrt{\frac{N^2}{4}+\bar{c}_1^2} - \sqrt{\frac{N^2}{4}+\bar{c}_3^2} - \frac{jd}{2}. \tag{32}$$

As pointed out by Ref. [90], solution of this equation for general values of i - j requires numerical evaluation. However, we soon show that this equation can be solved analytically for the case of small currents, $I \ll 1$.

E. Current-voltage relation

Before considering the limiting case, $I \ll 1$, we first derive the current-voltage (I - V) response of the general case. The potential difference across the system, $\Delta\phi$, is equal to minus the potential drop across the system, $-V$. These are both just a sum of potential differences in each region and the Donnan potential differences at the two interfaces ($x = \Delta_1, \Delta_2$)

$$-V = \Delta\phi = \Delta\phi_1 + \Delta\phi_2 + \Delta\phi_3 + \Delta\phi_{\text{don},1} + \Delta\phi_{\text{don},2}. \tag{33}$$

Using Eq. (22) yields the potential drops in regions 1 and 3

$$\begin{aligned} \Delta\phi_1 &= \phi_1(x=\Delta_1) - \phi_1(x=0) = (i/j)\ln\bar{c}_1, \\ \Delta\phi_3 &= \phi_3(x=\Delta_3) - \phi_3(x=\Delta_2) = -(i/j)\ln\bar{c}_3. \end{aligned} \tag{34}$$

Integrating Eq. (24) yields the potential drop in region 2

$$\Delta\phi_2 = \phi_2(x=\Delta_2) - \phi_2(x=\Delta_1) = -N^{-1}(jd + 2\bar{c}_{23} - 2\bar{c}_{21}). \tag{35}$$

Using the continuity of the positive electrochemical potential [Eq. (29)] yields the Donnan potential

$$\Delta\phi_{\text{don},1} = \ln\left(\frac{\bar{c}_1}{\bar{c}_{21}+N}\right), \quad \Delta\phi_{\text{don},2} = \ln\left(\frac{\bar{c}_{23}+N}{\bar{c}_3}\right). \tag{36}$$

Thus, substituting Eqs. (34)–(36) into (33) yields the I - V relation

$$-V = \Delta\phi = \left(\frac{i}{j}+1\right)\ln\frac{\bar{c}_1}{\bar{c}_3} + \ln\left(\frac{\bar{c}_{23}+N}{\bar{c}_{21}+N}\right) - \frac{jd + 2\bar{c}_{23} - 2\bar{c}_{21}}{N}. \tag{37}$$

Given a known geometry and known excess N counterion concentration, solution of Eqs. (32) and (37) requires numerical evaluation while for the extreme cases of ideal ($N \gg 1$) and vanishing ($N \ll 1$) permselectivity we have exact analytical solutions with simple expressions for the concentration, electrical potential and I - V relation [50,51].

F. Small current ($I \ll 1$) approximation

To derive the small current approximation ($I \ll 1$), we leverage the definition of the transport number [and Eq. (17)]

$$\tau = \frac{j_+}{j_+ - j_-} = \frac{\frac{1}{2}(j_+ + j_-) + \frac{1}{2}(j_+ - j_-)}{j_+ - j_-} = \frac{1}{2}\left(1 + \frac{j}{i}\right) = \frac{1}{2}\left(1 + \frac{J}{I}\right). \tag{38}$$

Alternatively, we write this as

$$\tau = \tfrac{1}{2} + \Delta\tau. \tag{39}$$

Both τ and $\Delta\tau$ are convenient notations and, for the sake of brevity, both are used in this work. Herein, we use

$$\frac{j}{i} = \frac{J}{I} = 2\Delta\tau. \tag{40}$$

Inserting Eq. (40) in Eq. (32) transforms the I - J relation into a I - τ relation. Then, we take the Taylor expansion of this I - τ relation [Eq. (32)] for the case of small current, $I \ll 1$. This yields to leading order an equation for τ (or $\Delta\tau$) whose solution is

$$\Delta\tau = N\left(2\sqrt{4+N^2} + 4\frac{\Sigma R_{\text{micro}}}{R_{\text{nano}}}\right)^{-1}, \tag{41}$$

where

$$R_{\text{nano}} = \frac{d}{hw}, \tag{42}$$

$$\Sigma R_{\text{micro}} = R_{\text{micro},1} + R_{\text{micro},3} + R_{FF,1} + R_{FF,3}, \tag{43}$$

$$R_{\text{micro},k} = \frac{L_k}{H_k W_k}, \tag{44}$$

$$R_{\text{FF},k} = 2f_k. \tag{45}$$

for $k = 1, 3$. Equation (42) is the nondimensional resistance attributed to the nanochannel without the effects of the surface charge [dimensional resistance, $\tilde{R}_{\text{nano}}$, given in Eq. (5)]. The notation ΣR_{micro} refers to all the resistances attributed to regions 1 and 3. This resistance, ΣR_{micro}, attributed to the microchannels has two terms. The first term is the ratio of the length to the cross-section area and is the simple microchannel resistance [Eq. (44)]. The second term relates how field lines focus in from a large geometry into the small permselective region [Eq. (45)]. Equation (43) is the nondimensional version of the dimensional $\widetilde{\Sigma R}_{\mathrm{micro}}$ in Eq. (6).

It indeed is easy to observe that $\Delta\tau$ ranges from 0 to $\frac{1}{2}$ (such that $\Delta\tau \in [0, \frac{1}{2}]$) as N increases from 0 to infinity such that $J(N \to 0) \to 0$ and $J(N \to \infty) \to I$ as expected for the vanishing and ideal permselective case, respectively. Similarly, τ takes values between $\frac{1}{2}$ to 1 (such that $\tau \in [\frac{1}{2}, 1]$). That $\Delta\tau$ (or τ) can be expressed solely as a function of the geometry and N is one of the main findings of this work. Our expression for τ also provides a conceptual correction to Ref. [90], which did not include the effects of field focusing in their expressions for τ [their Eqs. (61) and (62)]. Also, our final expression has a simpler and more intuitive form than theirs.

Equations (39)–(41) determines the I - J (or I - τ) relation in an explicit manner. As such the concentration and electrical potential distributions in regions 1 and 3 [Eqs. (18)–(22)] are explicitly known for the Ohmic response such that numerical evaluation is not required.

G. Ohmic resistance

Taking the Taylor approximation of the general I - V relation [Eq. (37)] for the case of small current, $I \ll 1$, and inserting Eqs. (40) and (41) yields

$$V = (2\tau - 1)I\bar{R}_{\mathrm{nano}} + \left[\tfrac{1}{2} + (\tau - \tfrac{1}{2})\sqrt{4N^{-2} + 1}\right] I\Sigma R_{\mathrm{micro}} \tag{46}$$

where

$$\bar{R}_{\mathrm{nano}} = R_{\mathrm{nano}}/N, \tag{47}$$

is the nondimensional nanochannel resistance that accounts for the effects of the surface charge and is related to the dimensional resistance given in Eq. (5). From Eq. (46), the Ohmic resistance of the system is

$$\begin{aligned} R_{\mathrm{unifying}} = R = \frac{V}{I} &= (2\tau - 1)\bar{R}_{\mathrm{nano}} \\ &+ \tfrac{1}{2}\left[1 + (2\tau - 1)\sqrt{4N^{-2} + 1}\right] \Sigma R_{\mathrm{micro}}. \end{aligned} \tag{48}$$

Equation (48), combined with Eq. (41), are the main findings of this work and provide an expression for the resistance for any value of N.

Inserting the various normalization parameters given throughout into Eqs. (41) and (48) yield the dimensional formulations of these equations (with $N = \tilde{N}/\tilde{c}_0$)

$$\tau = \frac{1}{2} + \frac{\tilde{N}}{\tilde{c}_0}\left(2\sqrt{4 + \frac{\tilde{N}^2}{\tilde{c}_0^2}} + 4\frac{\widetilde{\Sigma R}_{\mathrm{micro}}}{\tilde{R}_{\mathrm{nano}}}\right)^{-1}, \tag{49}$$

$$\begin{aligned} \tilde{R}_{\mathrm{unifying}} &= (2\tau - 1)\bar{\bar{\tilde{R}}}_{\mathrm{nano}} \\ &+ \frac{1}{2}\left[1 + (2\tau - 1)\sqrt{4\frac{\tilde{c}_0^2}{\tilde{N}^2} + 1}\right] \widetilde{\Sigma R}_{\mathrm{micro}}. \end{aligned} \tag{50}$$

It should be noted that the normalization for $\tilde{f}$ changes from 3D to 2D similar to how the current normalization changes [see paragraph below Eq. (21)]. In 3D, the total microchannel resistance (for symmetric channels) is

$$\widetilde{\Sigma R}_{\mathrm{micro}} = 2\tilde{\rho}_{\mathrm{res}}\left(\frac{\tilde{L}}{\tilde{H}\tilde{W}} + \frac{\tilde{f}}{\tilde{L}}\right). \tag{51}$$

While in a 2D problem, this resistance is given by

$$\widetilde{\Sigma R}_{\mathrm{micro}} = 2\tilde{\rho}_{\mathrm{res}}\left(\frac{\tilde{L}}{\tilde{H}} + \tilde{f}\right). \tag{52}$$

This difference in normalizations is discussed thoroughly in Refs. [50,51].

IV. DISCUSSION—UNIFYING SOLUTION

Here we discuss the advantages and shortcomings of the newly derived analytical model, $\tilde{R}_{\mathrm{unifying}}$ [Eqs. (49) and (50)], for the Ohmic response of a 3D system, which holds for all values of $\tilde{N}$ and $\tilde{c}_0$, and accounts for the effects of the microchannels. Thereafter, we demonstrate how this model can be extended to cylindrical nanopore geometries.

Shortcomings. Albeit a conceptual complication, there are no shortcomings.

Equations (3) and (4) suggest that in the limiting cases of vanishing and ideal permselectivity, the response could be described by a simple electrical circuit. This is not apparent upon substitution of Eq. (49) into Eq. (50) whereby the resultant expression is complicated and depends nonlinearly on $\widetilde{\Sigma R}_{\mathrm{micro}}$ and $\tilde{R}_{\mathrm{nano}}$. To circumvent this issue, we suggest not to view the final result as a single equation, which is perhaps an oversimplification. Consider that, in Eqs. (3) and (4), the transport number is enforced *a priori* as a hidden assumption. The resistances in Eqs. (3) and (4) are entirely determined on this number. Thus, if Eqs. (3) or (4) were to be presented in a detailed manner, then each of their according transport numbers needs to be presented separately such that each model requires two equations separately (i.e., $\tilde{R}_{3,\text{ideal}}$ and $\tau_{3,\text{ideal}} = 1$, and $\tilde{R}_{3,\text{vanishing}}$ and $\tau_{3,\text{vanishing}} = \frac{1}{2}$). Hence, the resolution is to view $\tilde{R}_{\text{unifying}}$ and τ as two separate variables, and, in this manner, the analysis is indeed as simple as the previous models. Accordingly, Eq. (50) can be treated as a series of weighted resistors that are connected together, whereby the weight is determined by the transport number [Eq. (49)]. Thus, the only apparent shortcoming has been circumvented and we are left to conclude that this model does not have any apparent shortcomings.

Advantages. This model provides analytical expressions for the two most essential properties of a permselective system, the Ohmic resistance [Eq. (50)] and the transport number [Eq. (49)], that depends on the entire geometry, and hold for all values of $\tilde{N}$ and $\tilde{c}_0$. Remarkably, the expressions for the transport number and the Ohmic resistance are a simple function of two nondimensional ratios: $N = \tilde{N}/\tilde{c}_0$ and $\widetilde{\Sigma R}_{\text{micro}}/\tilde{R}_{\text{nano}}$. The correspondence of Eq. (50) for all values of $\tilde{c}_0$ and geometries in 1D-2D simulations (Figs. 3 and 4) and 3D experiments (Fig. 5) is outstanding. Also, we show below that Eq. (50) reduces to Eqs. (2)–(4) at each of the appropriate limits. Hence $\tilde{R}_{\text{unifying}}$ is a master solution that unifies three models. In addition to numerical simulations, our theoretical modeling provides additional credibility to $\tilde{R}_{1,\text{Donnan}}$ over $\tilde{R}_{1,\text{super}}$ (Fig. 3).

Reproducing leading models. Using the normalizations provided throughout this work, we show that the nondimensional $\tilde{R}_{\text{unifying}}$ reproduces the *nondimensional* form of the other models presented in Sec. II.

One-layer system—Donnan equilibrium. For the case of the one-layer system, i.e., there are no microchannels ($\Sigma R_{\text{micro}} = 0$), Eq. (48) reduces to

$$R_{\text{unifying}}(\Sigma R_{\text{micro}} = 0) = R_{1,\text{Donnan}} = \frac{d}{hw}\frac{1}{\sqrt{4 + N^2}}. \quad (53)$$

This is the nondimensional form of Eq. (2).

Three-layer system—Ideal permselectivity. For the ideal permselective case ($N \gg 1$ and $\tau = 1$), the square bracket in Eq. (48) goes to unity as $N \to \infty$ and $\tau = 1$ [or $\Delta\tau = 0.5$ – Eq. (41)] such that Eq. (48) reduces to the known limit [50–52]

$$R_{\text{unifying}}(N \to \infty) = R_{3,\text{ideal}} = \bar{R}_{\text{nano}} + \Sigma R_{\text{micro}}. \quad (54)$$

This is the nondimensional form of Eq. (4).

Three-layer system —Vanishing permselectivity. For the case of vanishing permselectivity, we take $N \to 0$. We take the Taylor series expansion of Eq. (41) in terms of N, which leads to

$$\Delta\tau_{N \ll 1} = \frac{N}{4[1 + \Sigma R_{\text{micro}}/R_{\text{nano}}]}. \quad (55)$$

Inserting this into Eq. (48) yields the known solution [50–52,96]

$$R_{\text{unifying}}(N \to 0) = R_{3,\text{vanishing}} = \tfrac{1}{2}(R_{\text{nano}} + \Sigma R_{\text{micro}}). \quad (56)$$

As expected, a factor ½ appears. This is due to the fact that the electric current is transported by two charge carriers, which reduces the resistance accordingly (i.e., $\tau_{3,\text{vanishing}} \cong 1/2$). Equation (56) is the nondimensional form of Eq. (3).

Nanopores. The derived unifying model can also be extended to systems with cylindrical nanopores. The resistance of the nanochannel is derived under the assumption of a 1D profile (see Sec. III D). Due to this 1D behavior, the total resistance is divided by a factor $\tilde{h}\tilde{w}$, which is the cross-section area of the channel while the current and current density are related by $\tilde{I} = \tilde{i} \cdot \tilde{h}\tilde{w}$ [Eq. (21)]. However, since the derivation is 1D, the multiplication by the area is not limited to a rectangular nanochannel and also cylindrical nanopore, of radius $\tilde{a}_{\text{nano}}$, can be considered such that the nanopore resistance and total current need to be modified such that

$$\tilde{R}_{\text{nano}} = \frac{\tilde{\rho}_{\text{res}}\tilde{d}}{\pi\tilde{a}_{\text{nano}}^2}, \quad \tilde{\bar{R}}_{\text{nano}} = \frac{\tilde{R}_{\text{nano}}}{N}, \quad (57)$$

$$\tilde{I} = \tilde{i} \cdot \pi\tilde{a}_{\text{nano}}^2. \quad (58)$$

Naturally, if the microchannels are also cylindrical then these resistances also require some modification

$$\tilde{R}_{\text{micro}} = \frac{\tilde{\rho}_{\text{res}}\tilde{L}}{\pi\tilde{a}_{\text{micro}}^2}. \quad (59)$$

However, the field-focusing resistances now take on a complicated form that depends on various Bessel functions [97]. In the extreme limit that $\tilde{a}_{\text{nano}}/\tilde{a}_{\text{micro}} \ll 1$, which is the case of most nanopore systems, these can be approximated by the classical access resistance [54,81,98]

$$\tilde{R}_{\text{FF}} = \frac{\tilde{\rho}_{\text{res}}}{4\tilde{a}_{\text{nano}}}. \quad (60)$$

Importantly, the form of Eq. (6) [and/or Eq. (43)] remains

$$\widetilde{\Sigma R}_{\text{micro}} = 2(\tilde{R}_{\text{micro}} + \tilde{R}_{\text{FF}}). \quad (61)$$

Then, Eqs. (57)–(61) can be inserted into Eqs. (49) and (50). Since the form of these equations remains unchanged then the “linear-decrease-to-saturation-to-linear-decrease” resistance paradigm, shown in Fig. 2(b), continues to hold. The sole difference is that the critical concentration where we see the additional increase of the resistance (Fig. 2) is pushed down to lower concentrations. This can be attributed to the total resistance being proportional to $\tilde{a}^2_{\text{nano}}$ whereas for the rectangular geometry it is proportional to $\tilde{h}\tilde{w}$. In the latter situation, only $\tilde{h}$ is considered small, while here $\tilde{a}^2_{\text{nano}}$ is much smaller. Also, in contrast to large membranes, it is important to realize that for nanopores where $\tilde{a}_{\text{nano}}/\tilde{a}_{\text{micro}} \ll 1$ it can be expected that $\tilde{R}_{\text{FF}}$ is never going to be negligible relative to the nanopore resistance at low concentrations.

Finally we note the following three comments. First, in this work we suggest a shift from the conductance paradigm to the resistance paradigm. Our reason for this is simple. When the effects of the nanochannels cannot be neglected, and generally they should not, then the resistance formulation provides a more intuitive physical description of a simple electrical circuit [Fig. 1(c)]. Second, throughout this work, for brevity, we refer to the permselective region as the nanochannel. However, the "nanochannel" can be replaced with any nanoporous material that exhibits permselectivity (as detailed above in the Introduction and demonstrated for the case of a nanopore) and the results still hold. Third, for the sake of simplicity, we consider here symmetric and binary electrolytes ($z_\pm = \pm 1$) with equal ionic diffusivities ($\tilde{D}_\pm = \tilde{D}$), e.g., KCl, yet our approach, with some additional mathematical complexity, can be extended to any electrolyte. Hence, the findings of this work are not limited to this chosen electrolyte or nanochannels. Rather the results of this work are robust.

V. CONCLUSIONS

This work focuses on the Ohmic resistance of a permselective nanochannel flanked by two microchannels. We review the shortcomings and advantages of four leading models whose properties are outlined in Table I. We show that one of these models is incorrect, and the remaining three models, while correct, suffer from certain limitations. To bypass these limitations, we reduce the number of embedded assumptions in the derivation and derive an analytical model that unifies these three models. This model corresponds perfectly to simulations (Figs. 3 and 4) and experiments (Fig. 5) for all geometries and concentrations.

This model holds for any nanoporous material used for the electrokinetic transport of ions. It provides analytical expressions for the two most essential properties of ion transport through a permselective system, the transport number and Ohmic resistance, without reverting to preliminary time-consuming numerical simulations or experiments. These findings can be used to improve and expedite the design of any system using permselective materials for ion transport. Most importantly, the physics of ion transport through nanoporous materials is clearer and easier to understand.

ACKNOWLEDGMENTS

Y.G. acknowledges the support of the Ilse Katz Institute for Nanoscale Science & Technology. R.A.-R. acknowledges financial support from Zvi Yanay fellowship.

APPENDIX: SIMULATION AND EXPERIMENTAL PARAMETERS

A. Simulation parameters

Table II provides the parameters used in the 1D and 2D simulations shown in Figs. 3 and 4, respectively. See Refs. [50,52] for more details regarding simulations.

TABLE II. Simulation parameters.

		1D simulations	2D simulations
Microchannel length	$\tilde{L}[\mu\text{m}]$	—	100
Nanochannel length	$\tilde{d}[\mu\text{m}]$	1000	300
Excess counterion concentration	$\tilde{N}[\text{mol/m}^3]$	0.76	0.76
Microchannel height	$\tilde{H}[\mu\text{m}]$	–	10
Nanochannel height	$\tilde{h}[\mu\text{m}]$	–	190
Relative permittivity	ε_r	80	80
Temperature	$\tilde{T}[\text{K}]$	298	298
Diffusion coefficient	$\tilde{D}[\text{m/s}^2]$	2×10^{-9}	10^{-9}

B. Experimental parameters

The 3D experimental data shown in Fig. 5 are taken from Ref. [52]. The microchannel geometry is $\tilde{L} = 2\,\text{mm}$, $\tilde{H} = 48\,\mu\text{m}$, and $\tilde{W} = 3.3\,\text{mm}$. The diffusion coefficient is $\tilde{D} = 2 \times 10^{-9}\,\text{m}^2/\text{s}$. Table III provides the geometric parameters for the nanochannel width and height with the length being $\tilde{d} = 350\,\mu\text{m}$. We note that the values of $\tilde{f}$ differs than those given in Ref. [52]. This is attributed to the issue of full cell and half cell described previously [see the paragraph between Eqs. (22) and (23)]. Here, the

TABLE III. Geometric information for the nanochannel and counterion concentration shown in Fig. 5. The ratio $\tilde{L}/\tilde{H}\tilde{W} = 0.124[10^5/\text{m}]$.

Nanochannel $\tilde{w}$ and $\tilde{h}$	$\frac{\tilde{d}}{\tilde{h}\tilde{w}}\left[\frac{10^5}{\text{m}}\right]$	$\frac{\tilde{f}}{\tilde{L}}\left[\frac{10^5}{\text{m}}\right]$	$\tilde{N}\left[\frac{\text{mol}}{\text{m}^3}\right]$
$\tilde{w}_1 = 2.37\,\text{mm}$, $\tilde{h} = 178\,\text{nm}$	8.29	0.0163	2.1
$\tilde{w}_2 = 0.94\,\text{mm}$, $\tilde{h} = 178\,\text{nm}$	20.9	0.056	1.66
$\tilde{w}_3 = 0.092\,\text{mm}$, $\tilde{h} = 190\,\text{nm}$	197	0.298	2.75
$\tilde{w}_4 = 0.046\,\text{mm}$, $\tilde{h} = 178\,\text{nm}$	422	0.514	2.42

additional factor of 2 is accounted for within $\tilde{f}$ while in Ref. [52], R_{FF} is defined as $\tilde{R}_{FF} = \tilde{f}$ (and not $\tilde{R}_{FF} = 2\tilde{f}$ as in this work). As such and importantly, the final result for the resistances models are identical.

[1] D. Stein, M. Kruithof, and C. Dekker, Surface-Charge-Governed Ion Transport in Nanofluidic Channels, Phys. Rev. Lett. **93**, 035901 (2004).

[2] A. Wolf and N. Reber, P. Yu. Apel, B. E. Fischer, and R. Spohr, Electrolyte transport in charged single ion track capillaries, Nucl. Instrum. Methods Phys. Res. Sect. B Beam Interact. Mater. At. **105**, 291 (1995).

[3] L.-J. Cheng and L. J. Guo, Rectified ion transport through concentration gradient in homogeneous silica nanochannels, Nano Lett. **7**, 3165 (2007).

[4] W. Guan, R. Fan, and M. A. Reed, Field-effect reconfigurable nanofluidic ionic diodes, Nat. Commun. **2**, 506 (2011).

[5] K. Raidongia and J. Huang, Nanofluidic ion transport through reconstructed layered materials, J. Am. Chem. Soc. **134**, 16528 (2012).

[6] S. X. Li, W. Guan, B. Weiner, and M. A. Reed, Direct observation of charge inversion in divalent nanofluidic devices, Nano Lett. **15**, 5046 (2015).

[7] E. Choi, K. Kwon, D. Kim, and J. Park, An electrokinetic study on tunable 3D nanochannel networks constructed by spatially controlled nanoparticle assembly, Lab Chip **15**, 512 (2015).

[8] E. Choi, K. Kwon, D. Kim, and J. Park, Tunable reverse electrodialysis microplatform with geometrically controlled self-assembled nanoparticle network, Lab Chip **15**, 168 (2015).

[9] J. Lao, R. Lv, J. Gao, A. Wang, J. Wu, and J. Luo, Aqueous stable Ti_3C_2 MXene membrane with fast and photoswitchable nanofluidic transport, ACS Nano **12**, 12464 (2018).

[10] J. Gamby, F.-D. Delapierre, A. Pallandre, B. Tribollet, C. Deslouis, and A.-M. Haghiri-Gosnet, Dielectric properties of a single nanochannel investigated by high-frequency impedance spectroscopy, Electrochem. Commun. **66**, 5 (2016).

[11] J. Wang, L. Zhang, J. Xue, and G. Hu, Ion diffusion coefficient measurements in nanochannels at various concentrations, Biomicrofluidics **8**, 024118 (2014).

[12] K. M. Weerakoon-Ratnayake, C. E. O'Neil, F. I. Uba, and S. A. Soper, Thermoplastic nanofluidic devices for biomedical applications, Lab Chip **17**, 362 (2017).

[13] R. Chein and B. Chung, Numerical study of ionic current rectification through non-uniformly charged micro/nanochannel systems, J. Appl. Electrochem. **43**, 1197 (2013).

[14] C. Wang, C. Miao, X. Zhu, X. Feng, C. Hu, D. Wei, Y. Zhu, C. Kan, D. N. Shi, and S. Chen, Fabrication of stable and flexible nanocomposite membranes comprised of cellulose nanofibers and graphene oxide for nanofluidic ion transport, ACS Appl. Nano Mater. **2**, 4193 (2019).

[15] R. B. Schoch, H. van Lintel, and P. Renaud, Effect of the surface charge on ion transport through nanoslits, Phys. Fluids **17**, 100604 (2005).

[16] R. B. Schoch and P. Renaud, Ion transport through nanoslits dominated by the effective surface charge, Appl. Phys. Lett. **86**, 253111 (2005).

[17] R. B. Schoch, J. Han, and P. Renaud, Transport phenomena in nanofluidics, Rev. Mod. Phys. **80**, 839 (2008).

[18] J. Feng, M. Graf, K. Liu, D. Ovchinnikov, D. Dumcenco, M. Heiranian, V. Nandigana, N. R. Aluru, A. Kis, and A. Radenovic, Single-layer MoS_2 nanopores as nanopower generators, Nature **536**, 197 (2016).

[19] C. Lee, L. Joly, A. Siria, A.-L. Biance, R. Fulcrand, and L. Bocquet, Large apparent electric size of solid-state nanopores due to spatially extended surface conduction, Nano Lett. **12**, 4037 (2012).

[20] E. Secchi, A. Niguès, L. Jubin, A. Siria, and L. Bocquet, Scaling Behavior for Ionic Transport and its Fluctuations in Individual Carbon Nanotubes, Phys. Rev. Lett. **116**, 154501 (2016).

[21] J. A. Manzanares, W. D. Murphy, S. Mafe, and H. Reiss, Numerical simulation of the nonequilibrium diffuse double layer in ion-exchange membranes, J. Phys. Chem. **97**, 8524 (1993).

[22] G. Yossifon, P. Mushenheim, Y.-C. Chang, and H.-C. Chang, Nonlinear current-voltage characteristics of nanochannels, Phys. Rev. E **79**, 046305 (2009).

[23] C. Duan and A. Majumdar, Anomalous ion transport in 2-nm hydrophilic nanochannels, Nat. Nanotechnol. **5**, 848 (2010).

[24] G. Yossifon, P. Mushenheim, Y.-C. Chang, and H.-C. Chang, Eliminating the limiting-current phenomenon by geometric field focusing into nanopores and nanoslots, Phys. Rev. E **81**, 046301 (2010).

[25] J. Yang, X. Zhang, F. Chen, and L. Jiang, Geometry modulation of ion diffusion through layered asymmetric graphene oxide membranes, Chem. Commun. **55**, 3140 (2019).

[26] X. Zhang, Q. Wen, L. Wang, L. Ding, J. Yang, D. Ji, Y. Zhang, L. Jiang, and W. Guo, Asymmetric electrokinetic proton transport through 2D nanofluidic heterojunctions, ACS Nano **13**, 4238 (2019).

[27] D. Ji, Q. Wen, L. Cao, Q. Kang, S. Lin, X. Zhang, L. Jiang, and W. Guo, Electrokinetically controlled asymmetric ion transport through 1D/2D nanofluidic heterojunctions, Adv. Mater. Technol. **4**, 1800742 (2019).

[28] R. Fan, S. Huh, R. Yan, J. Arnold, and P. Yang, Gated proton transport in aligned mesoporous silica films, Nat. Mater. **7**, 303 (2008).

[29] J.-J. Shao, K. Raidongia, A. R. Koltonow, and J. Huang, Self-assembled two-dimensional nanofluidic proton channels with high thermal stability, Nat. Commun. **6**, 7602 (2015).

[30] T. Li, S. X. Li, W. Kong, C. Chen, E. Hitz, C. Jia, J. Dai, X. Zhang, R. Briber, Z. Siwy, M. Reed, and L. Hu, A nanofluidic ion regulation membrane with aligned cellulose nanofibers, Sci. Adv. **5**, eaau4238 (2019).

[31] S.-H. Lee, H. Lee, T. Jin, S. Park, B. J. Yoon, G. Y. Sung, K.-B. Kim, and S. J. Kim, Sub-10nm transparent all-around-gated ambipolar ionic field effect transistor, Nanoscale **7**, 936 (2015).

[32] R. M. M. Smeets, U. F. Keyser, D. Krapf, M.-Y. Wu, N. H. Dekker, and C. Dekker, Salt dependence of ion transport and DNA translocation through solid-state nanopores, Nano Lett. **6**, 89 (2006).

[33] W. Kong, C. Wang, C. Jia, Y. Kuang, G. Pastel, C. Chen, G. Chen, S. He, H. Huang, J. Zhang, S. Wang, L. Hu, Muscle-Inspired Highly Anisotropic, and Ion-Conductive Hydrogels Strong. Adv. Mater. **30**, 1801934 (2018).

[34] Z. Zhang, S. Yang, P. Zhang, J. Zhang, G. Chen, and X. Feng, Mechanically strong MXene/Kevlar nanofiber composite membranes as high-performance nanofluidic osmotic power generators, Nat. Commun. **10**, 1 (2019).

[35] L. Ding, D. Xiao, Z. Lu, J. Deng, Y. Wei, J. Caro, and H. Wang, Oppositely charged Ti_3C_2Tx MXene membranes with 2D nanofluidic channels for osmotic energy harvesting, ACS Nano **13**, 8917 (2019).

[36] S. Hong, F. Ming, Y. Shi, R. Li, I. S. Kim, C. Y. Tang, H. N. Alshareef, and P. Wang, Two-dimensional Ti_3C_2Tx MXene membranes as nanofluidic osmotic power generators, ACS Nano **13**, 8917 (2019).

[37] Q.-Y. Wu, C. Wang, R. Wang, C. Chen, J. Gao, J. Dai, D. Liu, Z. Lin, and L. Hu, Salinity-gradient power generation with ionized wood membranes, Adv. Energy Mater. **10**, 1902590 (2020).

[38] W. Xin, Z. Zhang, X. Huang, Y. Hu, T. Zhou, C. Zhu, X.-Y. Kong, L. Jiang, and L. Wen, High-performance silk-based hybrid membranes employed for osmotic energy conversion, Nat. Commun. **10**, 1 (2019).

[39] L. Duan and L. Yobas, Label-free multiplexed electrical detection of cancer markers on a microchip featuring an integrated fluidic diode nanopore array, ACS Nano **12**, 7892 (2018).

[40] W. Hirunpinyopas, P. Iamprasertkun, M. A. Bissett, and R. A. W. Dryfe, Tunable charge/size selective ion sieving with ultrahigh water permeance through laminar graphene membranes, Carbon **156**, 119 (2020).

[41] K. Saha, J. Deka, and K. Raidongia, Energy from the nanofluidic transport of water through nanochannels between packed silica spheres, ACS Appl. Nano Mater. **2**, 5850 (2019).

[42] G. Chen, T. Li, C. Chen, C. Wang, Y. Liu, W. Kong, D. Liu, B. Jiang, S. He, Y. Kuang, and L. Hu, A highly conductive cationic wood membrane, Adv. Funct. Mater. **29**, 1902772 (2019).

[43] Q. Liu, Y. Liu, B. Lu, Y. Wang, Y. Xu, J. Zhai, and X. Fan, A high rectification ratio nanofluidic diode induced by an "ion pool, " RSC Adv. **10**, 7377 (2020).

[44] Y. Ma, M. Sun, X. Duan, A. van den Berg, J. C. T. Eijkel, and Y. Xie, Dimension-reconfigurable bubble film nanochannel for wetting based sensing, Nat. Commun. **11**, 1 (2020).

[45] Y. Zhou, C. Chen, X. Zhang, D. Liu, L. Xu, J. Dai, S.-C. Liou, Y. Wang, C. Li, H. Xie, Q. Wu, B. Foster, T. Li, R. M. Briber, and L. Hu, Decoupling ionic and electronic pathways in low-dimensional hybrid conductors, J. Am. Chem. Soc. **141**, 17830 (2019).

[46] M. Zhao, Y. Liu, and B. Su, Anomalous proton transport across silica nanochannel membranes investigated by ion conductance measurements, Anal. Chem. **91**, 13433 (2019).

[47] S. Prakash and A. T. Conlisk, Field effect nanofluidics, Lab Chip **16**, 3855 (2016).

[48] L. Bocquet and E. Charlaix, Nanofluidics, from bulk to interfaces, Chem. Soc. Rev. **39**, 1073 (2010).

[49] P. Liu, Y. Sun, C. Zhu, B. Niu, X. Huang, X.-Y. Kong, L. Jiang, and L. Wen, Neutralization reaction assisted chemical-potential-driven ion transport through layered titanium carbides membrane for energy harvesting, Nano Lett. (2020).

[50] Y. Green, S. Shloush, and G. Yossifon, Effect of geometry on concentration polarization in realistic heterogeneous permselective systems, Phys. Rev. E **89**, 043015 (2014).

[51] Y. Green, Y. Edri, and G. Yossifon, Asymmetry-induced electric current rectification in permselective systems, Phys. Rev. E **92**, 033018 (2015).

[52] Y. Green, R. Eshel, S. Park, and G. Yossifon, Interplay between nanochannel and microchannel resistances, Nano Lett. **16**, 2744 (2016).

[53] I. Vlassiouk, S. Smirnov, and Z. Siwy, Ionic selectivity of single nanochannels, Nano Lett. **8**, 1978 (2008).

[54] A. Alcaraz, M. L. López, M. Queralt-Martín, and V. M. Aguilella, Ion transport in confined geometries below the nanoscale: Access resistance dominates protein channel conductance in diluted solutions, ACS Nano **11**, 10392 (2017).

[55] G. Yossifon and H.-C. Chang, Selection of Nonequilibrium Overlimiting Currents: Universal Depletion Layer Formation Dynamics and Vortex Instability, Phys. Rev. Lett. **101**, 254501 (2008).

[56] S. M. Rubinstein, G. Manukyan, A. Staicu, I. Rubinstein, B. Zaltzman, R. G. H. Lammertink, F. Mugele, and M. Wessling, Direct Observation of a Nonequilibrium Electro-Osmotic Instability, Phys. Rev. Lett. **101**, 236101 (2008).

[57] I. Rubinstein and B. Zaltzman, Equilibrium Electroconvective Instability, Phys. Rev. Lett. **114**, 114502 (2015).

[58] R. Abu-Rjal, I. Rubinstein, and B. Zaltzman, Driving Factors of Electro-Convective Instability in Concentration Polarization, Phys. Rev. Fluids **1**, 023601 (2016).

[59] R. Abu-Rjal, L. Prigozhin, I. Rubinstein, and B. Zaltzman, Equilibrium electro-convective instability in concentration polarization: The effect of non-equal ionic diffusivities and longitudinal flow, Russ. J. Electrochem. **53**, 903 (2017).

[60] D. Brogioli, Extracting Renewable Energy from a Salinity Difference Using a Capacitor, Phys. Rev. Lett. **103**, 058501 (2009).

[61] F. La Mantia, M. Pasta, H. D. Deshazer, B. E. Logan, and Y. Cui, Batteries for efficient energy extraction from a water salinity difference, Nano Lett. **11**, 1810 (2011).

[62] F. H. J. van der Heyden, D. J. Bonthuis, D. Stein, C. Meyer, and C. Dekker, Power generation by pressure-driven transport of ions in nanofluidic channels, Nano Lett. **7**, 1022 (2007).

[63] Z. S. Siwy and S. Howorka, Engineered voltage-responsive nanopores, Chem. Soc. Rev. **39**, 1115 (2010).

[64] R. Karnik, R. Fan, M. Yue, D. Li, P. Yang, and A. Majumdar, Electrostatic control of ions and molecules in nanofluidic transistors, Nano Lett. **5**, 943 (2005).

[65] R. Karnik, C. Duan, K. Castelino, H. Daiguji, and A. Majumdar, Rectification of ionic current in a nanofluidic diode, Nano Lett. **7**, 547 (2007).

[66] R. Yan, W. Liang, R. Fan, and P. Yang, Nanofluidic diodes based on nanotube heterojunctions, Nano Lett. **9**, 3820 (2009).

[67] Y. Green, Current-voltage response for unipolar funnel-shaped nanochannel diodes, Phys. Rev. E **98**, 033114 (2018).

[68] D. Branton *et al.*, The potential and challenges of nanopore sequencing, Nat. Biotech. **26**, 1146 (2008).

[69] A. Meller, L. Nivon, and D. Branton, Voltage-Driven DNA Translocations Through a Nanopore, Phys. Rev. Lett. **86**, 3435 (2001).

[70] B. Nadler, Z. Schuss, U. Hollerbach, and R. S. Eisenberg, Saturation of conductance in single ion channels: The blocking effect of the near reaction field, Phys. Rev. E **70**, 051912 (2004).

[71] A. Meller, A new tool for cell signalling research, Nat. Nanotechnol. **14**, 732 (2019).

[72] M. Aramesh, C. Forró, L. Dorwling-Carter, I. Lüchtefeld, T. Schlotter, S. J. Ihle, I. Shorubalko, V. Hosseini, D. Momotenko, T. Zambelli, E. Klotzsch, and J. Vörös, Localized detection of ions and biomolecules with a force-controlled scanning nanopore microscope, Nat. Nanotechnol. **14**, 791 (2019).

[73] M. Wanunu, W. Morrison, Y. Rabin, A. Y. Grosberg, and A. Meller, Electrostatic focusing of unlabelled DNA into nanoscale pores using a salt gradient, Nat. Nanotechnol. **5**, 160 (2010).

[74] M. Wanunu, T. Dadosh, V. Ray, J. Jin, L. McReynolds, and M. Drndić, Rapid electronic detection of probe-specific microRNAs using thin nanopore sensors, Nat. Nanotechnol. **5**, 807 (2010).

[75] M. Wanunu, J. Sutin, and A. Meller, DNA profiling using solid-state nanopores: Detection of DNA-binding molecules, Nano Lett. **9**, 3498 (2009).

[76] Y. Qiu, R. A. Lucas, and Z. S. Siwy, Viscosity and conductivity tunable diode-like behavior for meso- and micropores, J. Phys. Chem. Lett. **8**, 3846 (2017).

[77] H. Li, Z. Song, X. Zhang, Y. Huang, S. Li, Y. Mao, H. J. Ploehn, Y. Bao, and M. Yu, Ultrathin, molecular-sieving graphene oxide membranes for selective hydrogen separation, Science **342**, 95 (2013).

[78] A. Siria, P. Poncharal, A.-L. Biance, R. Fulcrand, X. Blase, S. T. Purcell, and L. Bocquet, Giant osmotic energy conversion measured in a single transmembrane boron nitride nanotube, Nature **494**, 455 (2013).

[79] P. M. Biesheuvel and M. Z. Bazant, Analysis of ionic conductance of carbon nanotubes, Phys. Rev. E **94**, 050601 (2016).

[80] Y. Green, S. Park, and G. Yossifon, Bridging the gap between an isolated nanochannel and a communicating multipore heterogeneous membrane, Phys. Rev. E **91**, 011002 (R) (2015).

[81] K. Lin, C.-Y. Lin, J. W. Polster, Y. Chen, and Z. S. Siwy, Charge inversion and calcium gating in mixtures of ions in nanopores, J. Am. Chem. Soc. **142**, 2925 (2020).

[82] S. Sohn, I. Cho, S. Kwon, H. Lee, and S. J. Kim, Surface conduction in a microchannel, Langmuir **34**, 7916 (2018).

[83] X. Nebavskaya, V. Sarapulova, D. Butylskii, C. Larchet, and N. Pismenskaya, Electrochemical properties of homogeneous and heterogeneous anion exchange membranes coated with cation exchange polyelectrolyte, Membranes **9**, 13 (2019).

[84] N. D. Pismenskaya, E. D. Melnikova, O. A. Rybalkina, and V. V. Nikonenko, The impact of long-time operation of an anion-exchange membrane AMX-Sb in the electrodialysis desalination of sodium chloride solution on the membrane current–voltage characteristic and the water splitting rate, Membr. Membr. Technol. **1**, 88 (2019).

[85] O. A. Rybalkina, K. A. Tsygurina, V. V. Sarapulova, S. A. Mareev, V. V. Nikonenko, and N. D. Pismenskaya, Evolution of current–voltage characteristics and surface morphology of homogeneous anion-exchange membranes during the electrodialysis desalination of alkali metal salt solutions, Membr. Membr. Technol. **1**, 107 (2019).

[86] W. Sparreboom, A. van den Berg, and J. C. T. Eijkel, Principles and applications of nanofluidic transport, Nat. Nanotechnol **4**, 713 (2009).

[87] I. Rubinstein and L. Shtilman, Voltage against current curves of cation exchange membranes, J. Chem. Soc. Faraday Trans. **2**, 231 (1979).

[88] I. Rubinstein, *Electro-Diffusion of Ions* (SIAM, Philadelphia, 1990).

[89] O. Schnitzer and E. Yariv, Electric conductance of highly selective nanochannels, Phys. Rev. E **87**, 054301 (2013).

[90] R. Abu-Rjal, V. Chinaryan, M. Z. Bazant, I. Rubinstein, and B. Zaltzman, Effect of concentration polarization on permselectivity, Phys. Rev. E **89**, 012302 (2014).

[91] S. J. Kim, Y.-C. Wang, J. H. Lee, H. Jang, and J. Han, Concentration Polarization and Nonlinear Electrokinetic Flow Near a Nanofluidic Channel, Phys. Rev. Lett. **99**, 044501 (2007).

[92] E. Yariv, Asymptotic current-voltage relations for currents exceeding the diffusion limit, Phys. Rev. E **80**, 051201 (2009).

[93] Y. Green, Approximate time-dependent current-voltage relations for currents exceeding the diffusion limit, Phys. Rev. E **101**, 043113 (2020).

[94] Y. Green and G. Yossifon, Effects of three-dimensional geometric field focusing on concentration polarization in a heterogeneous permselective system, Phys. Rev. E **89**, 013024 (2014).

[95] I. Rubinstein, Electroconvection at an electrically inhomogeneous permselective interface, Phys. Fluids Fluid. Dyn. **3**, 2301 (1991).

[96] Y. Green and G. Yossifon, Time-dependent ion transport in heterogeneous permselective systems, Phys. Rev. E **91**, 063001 (2015).

[97] I. Rubinstein and F. Maletzki, Electroconvection at an electrically inhomogeneous permselective membrane surface, J. Chem. Soc. Faraday Trans. **87**, 2079 (1991).

[98] J. E. Hall, Access resistance of a small circular pore, J. Gen. Physiol. **66**, 531 (1975).

Correction: Minor errors in Eqs. (34) and (35) have been fixed and an error introduced in Eq. (43) during production has been rectified.